

See discussions, stats, and author profiles for this publication at: <https://www.researchgate.net/publication/231674131>

# Complex Pattern Formation in Drying Dispersions

ARTICLE *in* LANGMUIR · NOVEMBER 2002

Impact Factor: 4.46 · DOI: 10.1021/la020491w

---

CITATIONS

30

---

READS

28

## 2 AUTHORS:



[Karine Mougín](#)

French National Centre for Scientific Research

35 PUBLICATIONS 353 CITATIONS

[SEE PROFILE](#)



[Dr. Hamidou Haidara](#)

French National Centre for Scientific Research

85 PUBLICATIONS 467 CITATIONS

[SEE PROFILE](#)

# Complex Pattern Formation in Drying Dispersions

K. Mougin and H. Haidara\*

*Institut de Chimie des Surfaces et Interfaces-ICSI-CNRS, 15 Rue Jean Starcky,  
B.P. 2488, F-68057 Mulhouse Cedex, France*

*Received May 28, 2002. In Final Form: September 10, 2002*

We investigated the formation of complex aggregation patterns during the drying of nanocolloidal dispersion drops on various surfaces. Our results show that large-scale and well-organized multibranched surface aggregates can form during this drying process. Both the emergence and topological features of these complex patterns were found to be controlled by two parameters: (1) the actual volume fraction of the drop in the late step of the drying and (2) the hydrodynamic shear involved in the rupture–dewetting and receding motion of the residual suspension drop. A simple phenomenological model was proposed, which accounts for the experimental results and their analogy with shear instabilities and structure formation in purposely designed Hele–Shaw cells.

## Introduction

Heterogeneous liquids are of central importance in biology (biodispersions) and basic technologies (emulsions, suspensions, and polymer solutions) where they are spread onto substrates, either as thin films or sprayed microdrops.<sup>1–4</sup> For volatile suspensions, the partial evaporation of the solvent or complete drying step required by the film processing may either result in random and featureless aggregates or lead to the formation of well-defined complex fractal structures at the surface.<sup>5–9</sup> For instance, such complex structures are known to form under certain specific conditions from the aggregation of viruses, proteins, or cells, during the drying of biodispersions on both patterned and homogeneous substrates. Therefore, understanding the underlying mechanisms and key parameters which govern the formation of these structures may provide an interesting route for the controlled elaboration of complex and fractal surface assemblies, which are of both fundamental and technological importance. The formation of complex patterns in flowing liquids in general, and especially in colloidal dispersions, was discovered about a century ago and known to be driven by hydrodynamic instabilities which develop in the moving interface.<sup>10,11</sup> The most commonly observed example of these interface instabilities is the formation of fingerlike patterns (fingering patterns), described a few decades ago by Saffman and Taylor. These interface instabilities, also known as Saffman–Taylor hydrodynamic instabilities, are essentially governed by the capillary number  $Ca \sim (\mu U/\gamma)$ , where  $\mu$ ,  $\gamma$ , and  $U$  represent the surface tension, the viscosity, and the velocity of the moving fluid,

respectively. On the other hand, hydrodynamic instabilities leading to the formation of multibranched fractal structures are rarely predictable and observed in wetting processes. So far, these arborescent fractal patterns have mainly been produced in a confined model two-dimensional (2-D) space represented by two parallel plates (the Hele–Shaw cell), during the displacement of a fluid–fluid interface. Despite their strong topological difference, both Saffman–Taylor instabilities and multibranched fractal fingering basically arise from the same hydrodynamic phenomenon described by Darcy's law,<sup>10</sup>

$$U(x,y) \approx -(h^2/\eta) \nabla p(x,y) \quad (1)$$

where  $U(x,y)$  is the averaged in-plane velocity related to the pressure gradient  $\nabla p(x,y)$  at the moving fluid interface in a two-dimensional flow;  $h$  and  $\eta$  denote the thickness (normal to the flow plane) and viscosity, respectively, of the confined fluid interface. This velocity is obtained at the limit of the lubrication approximation with a no-slip condition at the solid–liquid interface, and it is assumed that all the pressure terms are equal to  $\nabla p(x,y)$ .<sup>12</sup> In this paper, we show that quite complex and fascinating fractal aggregation structures, in all similar to the ones produced in the celebrated Hele–Shaw cell, can readily emerge during the drying of colloidal dispersions at chemically homogeneous and topologically uniform substrates, whenever certain conditions (though specific) are satisfied. The mechanisms and critical parameters which control the formation and the organization of these colloidal aggregates into large-scale complex surface patterns are herein investigated during the drying of nanocolloidal dispersion drops.

## Experimental Section

The colloidal particles were tetrachloroauric(III) acid hydrate,  $[HAuCl_4] \cdot H_2O$ , stabilized with citric acid trisodium in an aqueous dispersion. When  $HAuCl_4$  is reduced with trisodium citrates, stabilized Au nanoparticles bearing the negative charge of the citrate ions are obtained,<sup>13–15</sup> for which the average size depends on the elaboration mode. For these experiments, suspensions of nanogold particles of average size  $25 \pm 5$  nm were elaborated and used at three different volume fractions in the aqueous

\* To whom correspondence should be addressed. Phone: +33 (0)3-89-60-88-39. Fax: +33 (0)3-89-60-87-99. E-mail: h.haidara@uha.fr.

- (1) Routh, A. F.; Russel, W. B.; Tang, J.; El-Aasser, M. S. *J. Coat. Technol.* **2001**, *73*, 41.
- (2) Kirsch, S.; Pfau, A.; Stubbs, J.; Sundberg, D. *Colloids Surf., A* **2001**, *183–185*, 725.
- (3) Wolde, P. R. T.; Frenkel, D. *Science* **1997**, *277*, 1975.
- (4) Baker, E. A.; Hunt, G. M.; Stevens, J. G. *Pestic. Sci.* **1983**, *14*, 645.
- (5) Parisse, F.; Allain, C. *Langmuir* **1997**, *13*, 3598.
- (6) Deegan, R. D., et al. *Nature* **1997**, *389*, 827.
- (7) Ben-Jacob, E.; Garik, P. *Nature* **1990**, *343*, 523.
- (8) Deegan, R. D. *Phys. Rev. E* **2000**, *61*, 475.
- (9) Haidara, H.; Mougin, K.; Schultz, J. *Langmuir* **2001**, *17*, 659.
- (10) Van Damme, H. *The Fractal Approach to Heterogeneous Chemistry*; Avnir, D., Ed.; John Wiley & Sons Ltd: Chichester, 1989; pp 199–226.
- (11) Schwabe, D.; Möller, U.; Schneider, J.; Scharmann, A. *Phys. Fluids A* **1992**, *4*, 2368.

(12) Haidara, H.; Vonna, L.; Schultz, J. *J. Chem. Phys.* **1997**, *107*, 630.

(13) Grabar, K. C.; Allison, K. J.; Baker, B. E.; Bright, R. M.; Brown, K. R.; Freeman, R. G.; Fox, A. P.; Keating, C. D.; Musick, M. D.; Natan, M. J. *Langmuir* **1996**, *12*, 2353.

(14) Li, W., et al. *Colloids Surf., A* **2000**, *175*, 217.

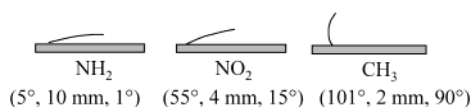


**Figure 1.** Wetting properties of the dispersion drop ( $\phi_{\text{ref}} \sim 1.5 \times 10^{-5}$ ) on various substrates. The triplet in parentheses corresponds to the equilibrium contact angle  $\theta_e$ , the contact diameter  $d$  at maximum spreading, and the receding contact angle  $\theta_r$ , respectively.

suspension: (1)  $\phi_{\text{ref}} \sim 1.5 \times 10^{-5}$ , (2)  $0.1\phi_{\text{ref}}$ , and (3)  $5\phi_{\text{ref}}$ . The reference suspension of volume fraction  $\phi_{\text{ref}} \sim 1.5 \times 10^{-5}$  corresponds to a concentration in weight (wt %) of  $[\text{HAuCl}_4] \cdot \text{H}_2\text{O}$  and citric acid trisodium of 0.03 and 0.02 wt %, respectively, for a pH of the final suspension of 6.5.

Three substrates consisting of self-assembled organosilane molecular films onto rigid silicon wafers were used for these experiments.<sup>15</sup> The organosilane compounds composing the molecular films were (1) methyl-terminated hexadecyltrichlorosilane (*hydrophobic compound referred to as  $\text{CH}_3$* ), (2) amine-terminated 6-aminopropyltrimethoxysilane (*hydrophilic electron acceptor compound referred to as  $\text{NH}_2$* ), and (3) nitrogen dioxide terminated 3-(2,4-dinitrophenylamino)propyltriethoxysilane (*hydrophilic electron donor compound referred to as  $\text{NO}_2$* ). The silicon substrates were first cleaned in piranha solution (3:7 v/v of a 30%  $\text{H}_2\text{O}_2$  and  $\text{H}_2\text{SO}_4$  mixture), thoroughly rinsed with deionized and twice distilled water, and then dried under nitrogen before silane coating. This treatment is aimed to produce a high surface silanol ( $\text{SiOH}$ ) density, to which functional silanes will adsorb upon hydrolysis. The homogeneous molecular films were obtained by vapor-phase deposition in a dynamically evacuated chamber (40 min at  $5 \times 10^{-3}$  Torr). The wafers were placed above a mixture of the organosilane (60  $\mu\text{L}$ ) in 3 mL of mineral oil, which was previously evacuated (de-aired). Though it gives macroscopic properties comparable to those of solvent-coated films, this vapor deposition prevents the organic layer from solvent-mediated incorporation of molecular scale contamination and defects. A labeled sketch representing the wetting parameters of the dispersion drop on these model surfaces, which are hereafter used in our study, are given in Figure 1, the values in parentheses representing the equilibrium contact angle  $\theta_e$ , the contact diameter  $d$ , and the receding contact angle  $\theta_r$ , respectively. The experiments properly consisted of depositing a dispersion drop of constant volume ( $\sim 8 \mu\text{L}$ ) on the substrates and allowing the drops to dry under ambient conditions ( $T = 20^\circ\text{C}$ , relative humidity  $\text{RH} = 33\%$ ). The drying kinetics was observed and recorded using an optical microscope equipped with a video-camera device. Under these experimental conditions, the evaporation rate of the dispersion drop  $v_E$  (determined by weighing its mass on a microbalance) and time scale  $t_E$  at complete drying were found to be comparable at both  $\text{NH}_2$  and  $\text{NO}_2$  substrates (typically  $v_E \sim 3 \mu\text{g/s}$  and  $t_E \sim 30$  min).

## Results and Discussion

The experimental results are shown in panels a, b, and c of Figure 2 for the reference dispersion drop ( $\phi_{\text{ref}} \sim 1.5 \times 10^{-5}$ ) on the three substrates and in panels d and e for dispersion drops of volume fraction  $0.1\phi_{\text{ref}}$  and  $5\phi_{\text{ref}}$ , respectively, at the structure-forming substrate  $\text{NH}_2$ . Panel a of Figure 2 is representative of the aggregation patterns observed at the bare  $\text{NH}_2$  substrate, whereas panels b and c of Figure 2 are typical of the bare  $\text{NO}_2$  and  $\text{CH}_3$  surfaces, respectively. The absence of aggregation patterns at  $\text{CH}_3$  surfaces is somehow trivial due to the high contact angle and too-low contact area of the dispersion drop, leading upon evaporation to the formation of a thick particle deposit at this nonwetted substrate. On the other hand, large-scale and quite symmetric multi-branched aggregates characterized by a  $\pi/2$  orientation of the secondary branches relative to main 4-fold ones (dendritelike feature) are formed at the hydrophilic and

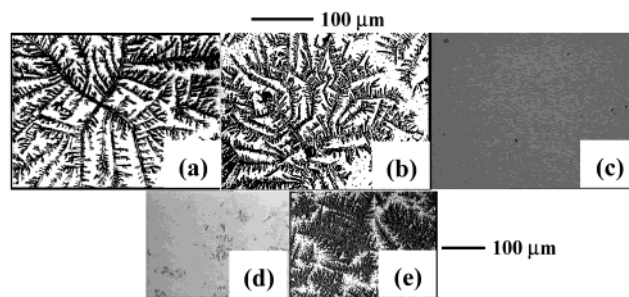


**Figure 2.** Aggregation patterns resulting from the drying of the reference volume fraction dispersion drop ( $\phi_{\text{ref}} \sim 1.5 \times 10^{-5}$ ) on the bare (a)  $\text{NH}_2$ , (b)  $\text{NO}_2$ , and (c)  $\text{CH}_3$  surfaces. The corresponding patterns for the dispersion drops of volume fractions  $\phi_v \sim 0.1\phi_{\text{ref}}$  and  $\phi_v \sim 5\phi_{\text{ref}}$  are given at the  $\text{NH}_2$  substrate in (d) and (e), respectively, for the same experimental conditions ( $T = 20^\circ\text{C}$ ,  $\text{RH} = 33\%$ ). Note the total absence of pattern on the dried zone left by the drop at  $\text{CH}_3$  surfaces (a), where only a residual thick and featureless particle deposit was observed, right above the dried drop (not represented here).

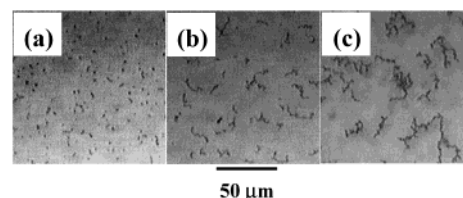


**Figure 3.** Snapshots showing the formation of the worm-shaped bulk aggregates and their structural evolution during the evaporation of the suspension drop ( $T = 20^\circ\text{C}$ ,  $\text{RH} = 33\%$ ): (a) spherical particles in the early stage ( $\sim 5$  min from the deposition of the  $8 \mu\text{L}$  drop); (b) wormlike clusters appearing in the intermediate stage ( $\sim 15$  min from the deposition of the drop); (c) interconnection of the wormlike clusters into larger size complex aggregates in the late stage of the evaporation ( $\sim 25$  min from the deposition of the drop).

more wetting  $\text{NH}_2$  and  $\text{NO}_2$  substrates. At these hydrophilic surfaces, the “dispersion/substrate” wetting parameters are such that an almost complete line pinning and confinement of the residual dispersion film appear in the late stage of the evaporation. The result in Figure 2d which involves the structure-forming amine substrate (*in the sense of its wetting properties*) clearly shows that the unique requirement of a low receding contact angle (see Figure 1) is not sufficient to account for the formation of the complex aggregation patterns observed in Figure 2b,c. Furthermore, the results suggest that the generation of complex aggregation patterns is critically controlled by the volume fraction of the dispersion. To gain further insights into the underlying mechanisms and critical parameters which control this pattern formation, we investigated the structural evolution of the dispersion within the bulk drop of volume fraction  $\phi = \phi_{\text{ref}}$  during evaporation. Representative snapshots of this time evolution are given in panels a, b, and c of Figure 3 in the early, intermediate, and late stages of the evaporation, respectively. These results show that interconnected wormlike clusters appear within the remaining drop, at both pattern-forming substrates ( $\text{NH}_2$  and  $\text{NO}_2$ ), in the late stage of the evaporation. On the other hand, neither the interconnected bulk clusters nor the complex surface patterns were observed during the evaporation-drying of lower volume fraction ( $0.1\phi_{\text{ref}}$ ) dispersion drops on the same substrates (see Figure 2d,  $\text{NH}_2$  substrate). These results clearly suggest that a threshold volume fraction ( $\phi_v$ ) exists, which should be reached during the evaporation, for both the interconnected bulk aggregates and complex surface patterns to appear at these structure-forming substrates.

(15) Mougin, K.; Haidara, H.; Castelein, G. *Colloids Surf., A* **2001**, *193*, 231.



One may thus reasonably think that the wormlike bulk aggregates constitute the initial seeds for the formation of the complex surface structures. Indirect evidence of the above conjuncture was brought by a complementary experiment where a larger drop volume ( $40\ \mu\text{L}$  against  $8\ \mu\text{L}$ ) of the dispersion of subcritical concentration ( $\phi = 0.1\phi_{\text{ref}}$ ) was deposited on an  $\text{NH}_2$ -terminated substrate. We could restore this way the emergence of both the interconnected wormlike bulk clusters and complex surface patterns. What this result shows is that beyond the nominal (initial) concentration, the parameter which actually controls the emergence of the bulk seeds and hence the formation of the complex surface patterns is the actual volume fraction of the drying drop in the late stage of the evaporation. What the above complementary experiment did by increasing the volume ( $v_0$ ) of the dispersion drop of subcritical nominal concentration  $\phi_0 = 0.1\phi_{\text{ref}}$  simply amounts to an increase of the number of particles ( $n_0$ ) in the reservoir. If  $v_p$  represents the average particle volume, this particle number follows the definition of the volume fraction as  $n_0 \sim (\phi_0 v_0 / v_p)$ . Since  $n_0$  is conserved during the drying, the concentration  $\phi$  of the evaporating drop, for which volume in the late stage of the drying is  $v$  ( $< v_0$ ), thus increases as  $\phi = (\phi_0 v_0) v^{-1}$ . As a result, the subcritical nominal concentration  $\phi_0$  of the initial dispersion drop is shifted toward the threshold value  $\phi_v^*$  where the interconnected wormlike clusters appear. Actually, the late-stage drop volume  $v$  at which the dewetting and related hydrodynamic effects set in is essentially a function of the substrate wetting properties and varies very little with the nominal concentration in the investigated interval of  $[10^{-1}, 5\phi_{\text{ref}}]$ . This explains why the actual volume fraction  $\phi$  lies below the threshold value  $\phi_v^*$  in the late stage of the evaporation, when smaller drop volumes  $v_0$  of a dispersion of low nominal concentration  $\phi_0$  are used (see Figure 2d,  $8\ \mu\text{L}$  dispersion drop,  $\phi_0 = 0.1\phi_{\text{ref}}$ , at  $\text{NH}_2$ -terminated surface). In this case, the late-stage drop volume  $v$  where dewetting sets in is reached for an actual volume fraction which is too low ( $\phi \sim \phi_0 v_0 v^{-1}$ ) for close particle–particle interactions to develop and allow the formation of the wormlike bulk clusters (particle sticking). Actually, this phenomenon is nothing else but the well-known concentration-dependent morphological transitions, usually observed in colloidal suspensions, and described by the standard “concentration–morphology” phase diagrams. The threshold volume fraction  $\phi_v^*$  is therefore characteristic of the colloidal suspension and depends, at a given temperature  $T$  and pressure  $p$ , on the diffusion length and particle–particle interactions (intermolecular, structural, and hydrodynamic interactions). In the late stage of the drying, the confined bulk seeds and accumulated free particles as well are submitted to the hydrodynamic shear within the retracting wedge of the remaining dispersion film, leading to the highly stretched arborescent surface patterns. Whenever the threshold volume fraction is reached in the evaporating drop, this late-stage hydrodynamics represents the critical step which controls the formation and topological feature of the surface aggregates. A more systematic experimental demonstration of this influence of the surface properties and related late-stage hydrodynamics on the aggregates’ topology is shown in Figures 4 and 5 for  $\text{NH}_2$  and  $\text{NO}_2$  substrates previously coated with the nanoparticles. The precoat was performed by immersing the substrates in the bulk dispersion for 1 h, allowing the nanoparticles to adsorb in quasi-equilibrium conditions. The samples were then washed in pure water to remove the excess dispersion, dried under nitrogen, and observed under atomic force microscopy (AFM) for the density and structure of the

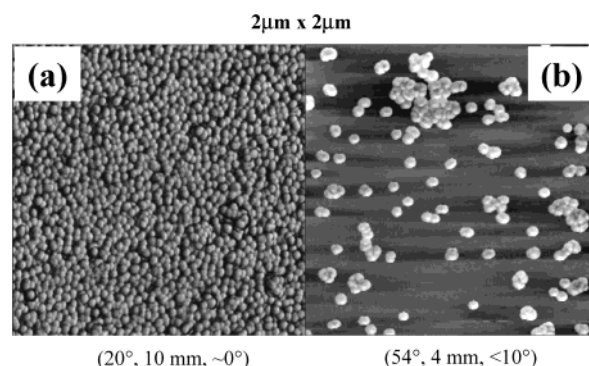


**Figure 4.** AFM pictures ( $0.5 \times 0.5\ \mu\text{m}$ ) and wetting parameters of the dispersion drop (equilibrium contact angle and diameter) at precoated (a)  $\text{NH}_2$  and (b)  $\text{NO}_2$  substrates.

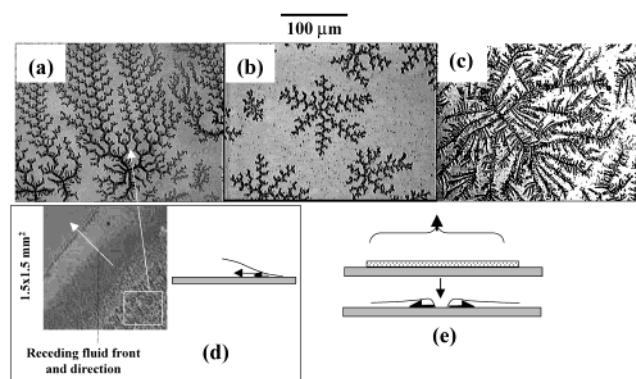


**Figure 5.** Aggregation patterns on the precoated substrates and their analogy with the flow asymmetry in Hele–Shaw cells. Shown in (a) and (b) are the asymmetrical and symmetrical patterns appearing at the periphery and at the center, respectively, of the drying drop at the precoated  $\text{NH}_2$  substrate; (c) shows the common topological feature observed on the precoated  $\text{NO}_2$  substrate. The symmetry of the flow and related shear is illustrated in (d), at the periphery of the receding macroscopic drop, and (e), at the center of the drop during the dewetting of the residual dispersion film.

adsorbed particle layers. The corresponding AFM images and wetting properties of the dispersion drop ( $\phi_{\text{ref}}$ ) are shown in panels a and b of Figure 4, respectively, for  $\text{NH}_2$ - and  $\text{NO}_2$ -terminated substrates, the values in parentheses standing for the same wetting parameters as in Figure 1. The extent of the surface coverage  $\Gamma$  during the coating is reasonably accounted for by the Gibbs equation  $\Gamma \sim s\phi_{\text{vi}} \exp[-\Delta F/kT]$ , where  $s$  and  $\phi_{\text{vi}}$  are the particle size and interface volume fraction and  $\Delta F$  is the free energy of adsorption. The low coverage at the electron donor  $\text{NO}_2$  surface is then straightforward, the interactions with the negatively charged particles being dominated by the repulsive electrostatic forces. On the other hand, the high coverage at  $\text{NH}_2$  surfaces results from the strong adsorption driven by the binding hydrogen and electrostatic interactions between the negatively charged particles and the electron acceptor  $\text{NH}_2$  groups (or their protonated ions  $\text{NH}_3^+$ ). The drying patterns at precoated  $\text{NH}_2$  substrates (panels a and b of Figure 5) clearly exhibit a higher structural order and topological richness, as compared to those produced on both the bare and precoated  $\text{NO}_2$  substrates (panel b of Figure 2 and panel c of Figure 5, respectively). In particular, the fractal patterns formed at the precoated  $\text{NH}_2$  substrates are composed of two distinct sets: the large-scale and highly stretched asymmetrical aggregates (fractal dimension  $D \sim 1.61$ )<sup>9</sup> and the small symmetrical aggregates (fractal dimension  $D \sim 2.03$ )<sup>9</sup> both formed by the repetition of hexagonal cell units

along the branches. The asymmetrical aggregates appear at the periphery of the receding drop, whereas symmetric aggregates appear in the late stage of the drying at the center of the drop, during the dewetting of the residual dispersion film. On the other hand, the low particle coverage at the precoated NO<sub>2</sub> does not seem to affect the topology of the aggregates, which in other respects does not display any dependence on their locus along the drop radius.

It then seems that once the required bulk criterion,  $\phi_{v*}$ , is satisfied, the whole morphological feature of the surface aggregates is determined by the late-stage hydrodynamics (retraction and rupture of the remaining film). The relevant parameters in this late stage are (1) the receding contact angle  $\theta_r$  of the macroscopic drop (or the moving ridge of the opening holes upon the rupture of the residual dispersion film) and (2) the surface topography (roughness and porosity) of the substrate. These parameters determine the magnitude of the shear-ordering stress experienced by both the confined bulk seeds and “free” particles within the remaining film. At difference with the Hele-Shaw cell where the fluid is symmetrically bounded by two rigid walls, the moving wedge here has a free liquid–air interface where we assume the interface tension gradient ( $\partial\gamma/\partial x$ ) to be negligible.<sup>12</sup> The unique pressure term at the solid–liquid interface is the viscous shear stress  $\tau$ , which is related in a unidirectional flow (along the  $x$  axis) to the pressure gradient ( $\partial p/\partial x$ ) of eq 1 by

$$\tau = h(\partial p/\partial x) \sim -3\eta(U/h^*) \sim -3\eta U/(h + b) \quad (2)$$

where  $\eta$  is the viscosity of the dispersion in the wedge,  $U$  is the average receding velocity of the flow, and  $h^* = (h + b)$ , the actual fluid thickness  $h$  in the receding wedge augmented by the eventual slippage of the particles at the substrate, characterized by length  $b$ . Expressing the actual fluid thickness  $h$  as a function of the lateral size  $l$  and receding angle  $\theta_r$  of the moving wedge leads to

$$\tau \sim -\eta U(kg\theta_r + b)^{-1} \quad (3)$$

A quantitative evaluation of eq 3 will require the accurate determination of  $b$  and  $l$ . Due to the intrinsic complexity of the systems which makes such a determination both experimentally and theoretically difficult, we have deliberately chosen to focus, in the following, on a qualitative discussion of our results, based on eq 3. At nonwetted and non-particle-attaching substrates<sup>15</sup> (CH<sub>3</sub> for instance), both higher  $\theta_r$  and slippage  $b$  are expected ( $\theta_r \gg 1$ ,  $b > 0$ , low  $\tau$ ). In this moving wedge, there is little confinement, and both the free particles and bulk seeds (if they exist) are simply collected within the receding drop, leading to the formation of a residual and featureless cluster. For completely wetted and particle-sticking substrates ( $tg\theta_r \sim \theta_r \ll 1$  rad,  $b \sim 0$ , high  $\tau$ ), both the wormlike bulk seeds and free particles are further confined and equally submitted to a higher magnitude shear-ordering stress within the receding wedge. As a result, the confined bulk seeds are further connected and stretched, leading upon the retraction of the fluid to the formation of the well-organized multibranched patterns. Furthermore, our results show that once the conditions for the formation of these complex surface patterns are satisfied, the topology (especially the structural ordering) of the resulting aggregates is critically determined by the topography of the underlying substrate. This is particularly illustrated at the precoated NH<sub>2</sub> substrate which actually constitutes a 2-D porous network (see Figure 4a and panels a and b of Figure 5). On these substrates, the

high hydrodynamic shear may be strongly coupled with the topography of the underlying network, driving the flow along some preferential “streamlines” of the porous bed. We do not expect interparticle attractive capillary forces<sup>16</sup> to play any significant role in the generation of these surface patterns, the size of the nanoparticles being smaller than the thickness of the aqueous film,<sup>17</sup> both at the periphery of the receding drop and in the residual thin film, just before it ruptures. We therefore think that the high structural order of these patterns, characterized by the repetition of hexagonal unit cells along the branches of the aggregates, is corrugated to the topography of the underlying lattice at the precoated NH<sub>2</sub> substrate. But yet, the explicit topological and length-scale correlations between the emerging order in the aggregation pattern (especially distance between branches or characteristic length of branches), on one hand, and the underlying surface network (particle size or arrangement) and the hydrodynamic flow, on the other hand, remain completely obscure. Further investigations based on model systems are therefore needed to better understand these correlations. Finally, our results show that the symmetry of the aggregates is strongly dependent on their locus in the drying spot (periphery or center), as illustrated in panels a and b of Figure 5. Furthermore, both aggregates have symmetry reminiscent of that of the flow and related shear, as observed in Hele-Shaw cells<sup>10</sup> where the flow configuration (axial or radial injection) determines the symmetry of the resulting patterns. The highly stretched aggregates which are located at the drop periphery are characteristic of the asymmetry of the flow and viscous shear associated with the inward retraction of the wedge. This is illustrated by the snapshot of the dewetting front in Figure 5d which shows both the location and preferential orientation of the structures along the flow lines (peripheral nucleation, inward propagation of branches). This is similar to the axial flow mode in Hele-Shaw cells. On the other hand, the symmetric aggregates which appear at the drop center are formed in the late stage of the drying, during the dewetting of the residual dispersion film. These aggregates are thus reminiscent of the axisymmetry of the flow and viscous shear around the nucleation point of the expanding dewetting holes, as depicted in Figure 5e. The latter process is in all respects similar to the radial flow in 2-D Hele-Shaw cells, which uniquely creates “symmetrical” multibranched and fractal patterns.

## Conclusion

We have studied the formation of complex aggregation patterns which arise during the evaporation-drying of nanosize colloidal dispersion drops on various substrates. Our results show that both the emergence and topological features of the surface patterns are controlled by two parameters. They are (1) the threshold volume fraction required for the formation of interconnected wormlike aggregates in the bulk suspension and (2) the surface properties of the underlying substrate. The interconnected bulk aggregates which form in the evaporating drop at the required threshold volume fraction were shown to provide the initial seeds for the formation of the complex surface patterns. The topography and wetting properties of the surface were shown to control, through the late-stage hydrodynamics, the whole morphology (structural order and symmetry) of the complex aggregation patterns.

LA020491W

(16) Denkov, N. D.; Veleev, O. D.; Kralchevsky, P. A.; Ivanov, I. B.; Yoshimura, H.; Nagayama, K. *Langmuir* **1992**, *8*, 3183.

(17) Maenosono, S.; Dushkin, C. D.; Saita, S.; Yamaguchi, Y. *Langmuir* **1999**, *15*, 957.